Evidence of Alveolar Macrophage Metabolic Shift Following Stereotactic Body Radiation Therapy -Induced Lung Fibrosis in Mice

Sarah Braga Cohen, Jeremy Lavigne, Morgane dos Santos, Georges Tarlet, Valerie Buard, Jan Baijer, Olivier Guipaud, Vincent Paget, Eric Deutsch, Mohamed-amine Benadjaoud, et al.

INTERNATIONAL JOURNAL OF
RADIATION ONCOLOGY • BIOLOGY • PHYSICS
www.redjournal.org

BIOLOGY CONTRIBUTION

Evidence of Alveolar Macrophage Metabolic Shift Following Stereotactic Body Radiation Therapy -Induced Lung Fibrosis in Mice

Sarah Braga-Cohen, PhD,[*] Jérémy Lavigne, PhD,[*] Morgane Dos Santos, PhD,[*] Georges Tarlet, BSc,[*] Valérie Buard, BSc,[*] Jan Baijer, PhD,[†] Olivier Guipaud, PhD,[*] Vincent Paget, PhD,[*] Eric Deutsch, MD, PhD,[‡,§] Mohamed Amine Benadjaoud, PhD,[*] Michele Mondini, PhD,[‡] Fabien Milliat, PhD,[*] and Agnès François, PhD[*]

[*]*Institut de Radioprotection et de Sûreté Nucléaire (IRSN), PSE-SANTE/SERAMED/LRAcc, F-92260 Fontenay-aux-Roses, France;* [†]*Plateforme de cytométrie, UMR Stabilité Génétique, Cellules souches et Radiations, CEA-INSERM-Universités de Paris et Paris-Sud, CEA-DRF/JACOB/iRCM/UMRE008-U1274, BP6 Fontenay-aux-Roses Cedex, France;* [‡]*INSERM U1030, Gustave Roussy, Université Paris-Saclay, Villejuif, France; and* [§]*Département d'Oncologie Radiothérapie, Gustave Roussy, Villejuif, France*

Received Feb 12, 2024; Accepted for publication Sep 4, 2024

Purpose: Radiation-induced pneumopathy is the main dose-limiting factor in cases of chest radiation therapy. Macrophage infiltration is frequently observed in irradiated lung tissues and may participate in lung damage development. Radiation-induced lung fibrosis can be reproduced in rodent models using whole thorax irradiation but suffers from limits concerning the role played by unexposed lung volumes in damage development.

Methods and Materials: Here, we used an accurate stereotactic body radiation therapy preclinical model irradiating 4% of the mouse lung. Tissue damage development and macrophage populations were followed by histology, flow cytometry, and single-cell RNA sequencing. Wild-type and CCR2 KO mice, in which monocyte recruitment is abrogated, were exposed to single doses of radiation, inducing progressive (60 Gy) or rapid (80 Gy) lung fibrosis.

Results: Numerous clusters of macrophages were observed around the injured area, during progressive as well as rapid fibrosis. The results indicate that probably CCR2-independent recruitment and/or in situ proliferation may be responsible for macrophage invasion. Alveolar macrophages experience a metabolic shift from fatty acid metabolism to cholesterol biosynthesis, directing them through a possible profibrotic phenotype. Depicted data revealed that the origin and phenotype of macrophages present in the injured area may differ from what has been previously described in preclinical models exposing large lung volumes, representing a potentially interesting trail in the deciphering of radiation-induced lung damage processes.

Conclusions: Our study brings new possible clues to the understanding of macrophage implications in radiation-induced lung damage, representing an interesting area for exploration in future studies.

Corresponding authors: Agnès François, PhD and Fabien Milliat, PhD; E-mail: fabien.milliat@irsn.fr, agnes.francois@irsn.fr

This protocol is registered with ClinicalTrials.gov and may be viewed online at https://clinicaltrials.gov/study/XXXXXX.

Disclosures: E.D. reports grants and personal fees from Roche Genentech; grants from Servier; grants from AstraZeneca; grants form Boehringer Ingelheim; grants and personal fees from Merck-Serono; grants from BMS; and grants from MSD outside the submitted work. M.M. reports grants from Boehringer Ingelheim and ACBiosciences outside the submitted work. This work was supported by the ROSIRIS program (IRSN funding); "INCA, Institut National du Cancer: "INCa 2018−1−PL BIO−06" and "INCa-SEQ-RTH22-n° Inca_16861" fundings. All other authors report no conflicts of interest.

Data Sharing Statement: Research data are stored in an institutional repository and will be shared on request to the corresponding author.

Supplementary material associated with this article can be found in the online version at doi:10.1016/j.ijrobp.2024.09.018.

Acknowledgments—We thank the Groupe de Soutien à l'Experimentation Animale (GSEA) from IRSN for their excellent support in animal care.

https://doi.org/10.1016/j.ijrobp.2024.09.018

Introduction

Lung toxicity is of concern for all thoracic malignancy radiation therapies (RTs). Radiation-induced lung damage is characterized by acute radiation pneumonitis (RP) and chronic radiation-induced lung fibrosis (RILF).[1,2] Radiation exposure and the generation of reactive oxygen/nitrogen species cause cell DNA damage and subsequent cell death, senescence, or activation in different lineages such as type I/II pneumocytes, endothelial cells, and macrophages.[3-5] Macrophages are an important component of lung immunity and represent the first line of defense against various traumatic situations and have been shown to be involved in numerous lung disease processes.[6] Lung macrophages are heterogeneous population with characteristics and roles driven by their location within the lung tissue (alveolar or interstitial) and have the possibility to acquire either classical or alternative activation, depending on the physiological or pathological changes in the tissue microenvironment.[7] High numbers of macrophages have been observed in radiation-induced lung damage, in both human samples after RT and preclinical models of whole thoracic irradiation (WTI), suggesting that they may play a role in lung response to radiation exposure.[8,9] Moreover, depletion of interstitial macrophages (IM) by CSF1R inhibition has been shown to prevent RILF following 16 Gy WTI in mice.[8] In preclinical models of WTI in mice, alveolar macrophages (AM) were depleted during the RP phase,[10] then repopulated during the RILF phase, forming organized clusters, considered implicated in fibrosis development.[11] Replenishment of resident macrophage populations has been shown to be caused by $CCR2^+$ monocyte recruitment, demonstrating that $CCR2^+$ infiltrating-derived macrophages participate in RILF.[12]

So far, WTI preclinical models have helped in the understanding of the potential roles played by various macrophage subpopulations in RP and RILF. It is known, however that the exposed volume is of paramount importance in the response of lung tissue to RT. Through the availability of dedicated small animal irradiators, exposure of very small volumes using millimetric beam collimation is now achievable, improving the clinical relevance of these new models.[13] We recently demonstrated that radiation-induced damage to 4% of mouse lung volume was associated with macrophage clusters developing around the injured area.[14,15] Once these macrophage clusters were noticed near radiation lesions, we investigated their phenotype and their origin. We postulated that the mechanisms involved in the response of limited lung volumes may differ from conventional preclinical models using whole- or hemi-thorax irradiation. Better knowledge of the physiopathological mechanisms associated with the irradiation of limited lung volumes will provide novel therapeutic opportunities to combat the side effects of thoracic RT.

In this study, we followed lung macrophage subpopulations in the mouse lung from 3 days to 12 months following a high-dose exposure of limited volume. We chose 2 different doses inducing progressive (60 Gy) and rapid (80 Gy) lung fibrosis. This choice was supported by previous studies characterizing this preclinical model in terms of volume and dose schedules (both single and fractionated doses) to obtain significant radiation-induced pneumonitis and fibrosis.[16,17] We used flow cytometry and single-cell RNA sequencing, giving us the opportunity to highlight interesting macrophage populations in the context of RP and RILF development in mice. Then, we used CCR2 knockout mice to determine if monocyte recruitment abrogation may influence radiation-induced damage severity. Our study provides new insights into the possible role of macrophages in the development of RP and RILF following the exposure of limited mouse lung volumes, suggesting that macrophage invasion results not only from both AM and IM recruitment from the bloodstream but also from in situ AM proliferation, with a switch toward a profibrotic metabolic state.

Methods

Experimental procedures

The following 3 different experimental procedures were used: (1) WT and CCR2 KO mice lung irradiation to 60 or 80 Gy for histologic studies (245 mice, 120 WT, and 125 CCR2 KO, between 5 and 8 mice per time point); (2) WT and CCR2 KO mice lung irradiation to 60 or 80 Gy for flow cytometry studies (267 mice, 142 WT and 125 CCR2 KO, between 5 and 8 mice per time point); and (3) WT and CCR2 KO mice lung irradiation to 60 or 80 Gy for single-cell RNA-seq studies (34 mice, between 4 and 6 mice per time point).

For histology and flow cytometry, tissues were harvested 3 days, 1 week, and 1, 3, 6, and 12 months postexposure. For single-cell RNA-seq experiments, tissues were harvested 1 and 6 months postexposure.

Animals and irradiation procedure

The 8-week-old male C57BL/6JRj (WT) mice were from Charles River and the CCR2 knockout mice (CCR2 KO, B6.129S4-Ccr2tm1Ifc/J) were from the Jackson Laboratory, bred in the IRSN animal facility and used at 8 weeks of age. The IRSN animal facility is accredited by the French Ministry of Agriculture. Animal experiments were performed in compliance with French and European regulations on the protection of animals used for scientific purposes (EC Directive 2010/63/EU and French Decree 2013−118). All experiments were approved by Ethics Committee #81 (approval number E92-032-01) and authorized by the French Ministry of Research (reference APAFiS#13021-2018011217442982 v1). This study was conducted according to Animal Research: Reporting of in vivo experiments (ARRIVE)

guidelines (https://arriveguidelines.org/arrive-guidelines accessed on 22 December 2022).

The Small Animal Radiation Research Platform (SARRP; XSTRAHL Ltd) was used to perform left lung focal exposure by arc therapy, using 3 × 3 mm beam collimation. Xstrahl carried out the commissioning of the SARRP platform and the calibration of the MuriPlan treatment planning system, using, for each collimator, a cylindrical ionization chamber for reference dose rate and EBT3 radiochromic films (Ashland ISP Advanced Materials) for depth doses and dose profiles. We then completed the characterization of the SARRP by making half-value layer measurements and reference dosimetry measurements with an ionization chamber, following the AAPM TG61 protocol.[18] EBT3 films were also used to measure dose profiles at different depths with 3 × 3 mm beam collimation. In our configuration, at 1 cm depth, the dose rate is about 2.3 Gy/min in dose to water.

For mice irradiation, profound anesthesia was induced to limit respiratory motion using 100 mg/kg ketamine (Imalgene 1000) and 10 mg/kg xylazine (Rompun 2%, Bayer Healthcare). The animals were immobilized on a restraint treatment bed. The isocenter was placed on the left lung on the cone beam computed tomography (CBCT) image using the treatment planning system MuriPlan, taking anatomical landmarks for reference. CBCT images were obtained using a 20 × 20 cm uncollimated beam (60 kV, 0.8 mA, inherent and additional filtration of 0.8 and 1 mm of beryllium and aluminum, respectively). A total of 236 projections were obtained, and a 3D reconstruction image of the mouse was transferred to the MuriPlan dose planning, verification, and delivery system. After image segmentation into air, lung, fat, tissue, and bone, we then placed the isocenter within the left lung. Irradiations were performed at 220 kV and 13 mA with inherent and additional filtrations of about 0.8 and 0.15 mm of beryllium and copper, respectively, and an half-value layer measurements of 0.667 mm of copper. Arc therapy treatment with an immobile stage and 220° gantry rotation from −110° to 110° was designed to deliver single doses of 60 Gy (inducing progressive lung fibrosis) or 80 Gy (inducing rapid lung fibrosis) (Fig. E1).[16]

Microcomputed tomography

Mice were anesthetized by inhalation of 1.5% isoflurane. Mouse lung imaging was performed using micro-CT Quantum GX2 (PerkinElmer) with respiratory gating at each study time point. Images were acquired at 90 kV, 88 μA, with additional filtration of 0.06 mm of copper + 0.5 mm of aluminum and with a field of view of about 36 mm with a reconstruction of 25 mm, allowing for a voxel size of 50 μm. The estimated shooting time was about 4 minutes, and 512 slices were acquired. The mean dose absorbed by the mice was about 900 mGy in dose to water.

The images were analyzed using AnalyzePro Software (AnalyseDirect, Inc), which allows for semiautomatic and manual segmentation. The semiautomatic mode was used to define airways and right and left lung volume, with the same threshold range for each mouse to be able to compare them. Lesions induced by irradiation—the injury patch—were manually contoured by the same operator. For each mouse, patch volume (when present) was then expressed as a percentage of the total lung volume (left lung + right lung + bronchi).

Based on these segmentations and to assess lung parenchyma, volumes were computed, and for each volume, Hounsfield Unit (HU) histograms were extracted using a bin width of 1-HU. For density distribution representation of the irradiated volume, smoothing curves were constructed using GraphPad Prism software applying second-order smoothing with 60 neighbors. As a second step, the volume of the left lungs, excluding bronchi but including the irradiated area, was analyzed using HU attenuation thresholds as described by Ruscitti et al[19] in the mouse, and more generally by Mecozzi et al.[20] Lung tissues were subdivided into normally aerated ([−900, −435] HU) and poorly aerated ([−435, +500] HU). To favor clarity in these graphs, control data were pooled as "young controls" corresponding to pooled 1- and 3-month data, serving as controls for the 3-day, 1-week, 1- and 3-month irradiated mice, and "old controls," corresponding to pooled 6 and 12 months control mice, serving as controls for 6- and 12-month irradiated mice. Finally, quantification of nonaerated volumes was realized by applying a threshold at −100 HU.

Histology and immunohistology

Tissue sections and immunostainings were performed as described in the Supplemental Materials and Methods.

Tissue digestion and flow cytometry analyses

Tissue digestion and the flow cytometry gating strategy are drawn from the bibliography (see Supplemental Materials and Methods and Figs. E2 and E3).[21,22]

Single-cell RNA-seq

Data preprocessing and most of the downstream analyses were performed using the Seurat Package of R software.[23] In total, 34 samples were included in the study: unirradiated (6 WT and 4 CCR2 KO), 60 Gy 1 month (4 WT and 4 CCR2 KO), 60 Gy 6 months (4 WT and 4 CCR2 KO), 80 Gy 1 month (4 WT), and 80 Gy 6M (4 WT). The first steps, from the sampling to the mechanical digestion, were the same as the flow cytometry protocol (see Supplemental Materials and Methods). As a reminder, a volume containing the injured patch plus margins ensuring both correct sampling (especially when the patch was not visible in macroscopy) and the removal of the injury-associated macrophages mainly located around the patch was dissected and harvested from the left lung and digested. A corresponding volume was harvested in unirradiated samples. After a red cell lysis step (Red blood cells lysis

buffer, Thermo Fisher, France), cells were resuspended in 90 μL of Phosphate-Buffered Saline (PBS) without Mg^{2+}/Ca^{2+}/0.5% BSA/2 mM ethylenediaminetetraacetic acid (EDTA) with 10 μL of CD45 Tumor-Infiltrating Leukocytes (TIL) MicroBeads (Miltenyi) and passed into magnetic separation (MS) columns (Miltenyi) to sort CD45-positive cells. For the encapsulation, we loaded 16,000 cells into a 10 × Chromium Controller (10 × Genomics), and scRNA-seq libraries were prepared using a single-cell 3′v3 Reagent Kit (10 × Genomics) according to the manufacturer's protocols. Library quantification and quality assessment were performed using the Agilent Bioanalyzer 2100 (Agilent Genomics). Indexed libraries were equimolarly pooled and sequenced on a NovaSEq 6000 sequencing system (Illumina Inc) with a minimum depth sequencing at 20,000 read pairs/cell. Single-cell RNA-seq outputs were processed using the Cell Ranger software (10 × Genomics). Analysis was performed using the Seurat Package (4.1.1) in R (4.1.3) and Monocle3 package (1.2.9) in R (4.2). Quality control metrics including those cells with <200 or >3000 transcripts profiled or presenting more than 15% of their transcriptome of mitochondrial origin were removed. For WT samples, we obtained 90,870 $CD45^+$ cells for Seurat quality control processes. When downsampling, we finally worked with 71,570 cells, that is, 14,314 cells per group. For CCR2 KO samples, we obtained 40,802 $CD45^+$ cells for Seurat quality control processes. After downsampling, we finally worked with 35,595 cells, that is, 11,865 cells per group.

For trajectory analysis using Monocle, we identified genes that change in expression as a function of pseudotime, using a multidirectional and multidimensional spatial autocorrelation, that is, the Moran's I test, provided by the graph_test function. This method allows us to find and classify genes that are differentially expressed across a single-cell trajectory, either on the entire trajectory or on only part of the trajectory focusing on some of the cells. The top 300 genes of each analysis were then injected in g:profiler, a web server functional enrichment analysis tool (https://biit.cs.ut.ee/gprofiler/gost). The enriched functional terms from Reactome and Kyoto Encyclopedia of Genes and Genomes (KEGG) database were extracted and classed according to the −log(10) of the adjusted *P* value False Discovery Rate (FDR). The entire script is given in Table E5.

Statistical analyses

GraphPad InStat 3 was used for statistical analyses. Data showing normal distribution with homogeneous variance were compared using unpaired Student *t* test to compare between 2 groups, and one-way analysis of variance with Tukey's post hoc for multiple comparison tests. Differences were considered significant at $P < .05$. Data are given as means ± standard error of the mean. The size of the groups was decided based on the laboratory's experience, with no randomization. Potential confounders were not controlled. No animal reached the a priori exclusion criteria. Analyses were performed in a nonblinded manner.

Results

Focal irradiation of the left lung is associated with macrophage invasion and impacts macrophage subpopulations

Both progressive (60 Gy) and rapid (80 Gy) fibrosis were associated with macrophage invasion of the injured area as shown by CD68 immunostaining (Fig. 1A), which were first characterized by flow cytometry. The gating strategy (Fig. E2) was based on results obtained on cells harvested from bronchoalveolar lavages to confirm macrophage subtypes (Fig. E3) and allowed AM ($CD45^+/CD11b^{+/-}/CD68^+/Ly6C^-/CD11c^+/SiglecF^+$), IM ($CD45^+/CD11b^+/CD68^+/Ly6C^-/CD11c^-/SiglecF^-$), M1 (classically activated $CD80^+$/MHC II^+), and M2 (alternatively activated $CD206^+$) distinction. A tendency to increase AM in a percentage of $CD45^+$ cells is observed after 60 and 80 Gy exposures (Fig. 1B). The percentage of IM seems to be increased only after 80 Gy exposure. AM showed a tendency to M1-like orientation, whereas IM showed a tendency to M2-like orientation (Fig. 1C).

Single-cell RNA-seq approach was used to access more precise information on macrophage subpopulations. Then, 90,870 viable $CD45^+$ leucocytes were analyzed from the lungs of WT mice 0, 60, and 80 Gy-irradiated 1 and 6 months postexposure (downsampled to 14,314 cells per group, Fig. E4A). We identified several known $CD45^+$ cells with the discrimination of 6 different cell types (Fig. 2A, left panel). Canonical markers are indicated in the heatmap (right panel). We next focused on 12,869 monocytes/macrophages, discriminating 6 subclusters using the Louvain method (Fig. 2B). Clusters were identified as AM, IM, dendritic cells, classical and nonclassical monocytes (C-mono and NC-mono), and 1 hybrid cluster. Both AM and IM are increased postirradiation (Fig. 2C). We next focused on 2,457 AM and IM from Figure 2B and obtained a new Uniform Manifold Approximation and Projection (UMAP) with 4 clusters shown in Figure 2D (left panel). Scores (6) identified clusters 0, 1, and 3 as AM and cluster 2 as IM (concerned cells in blue, Fig. 2D, middle and right panels, respectively, scores in Fig. E3B). The recruited macrophage score (Fig. 2E, left panel, Fig. E4B) identified cells in both IM and AM clusters. The ridge and violin plots (Fig. 2E, right panels) show that cluster 2 (IM) is the most concerned by the "recruited" profile. We thus decided to abrogate monocyte recruitment using CCR2 KO mice and followed tissue response to irradiation compared with WT mice.

The kinetics of radiation-induced focal lung damage in CCR2 KO mice is globally similar to WT as observed by CBCT images

Tissue consolidation was visible in CBCT images and 3D reconstructions in both WT and CCR2 KO mice 12 months post-60 Gy and as soon as 1 month post-80 Gy (Fig. 3A).

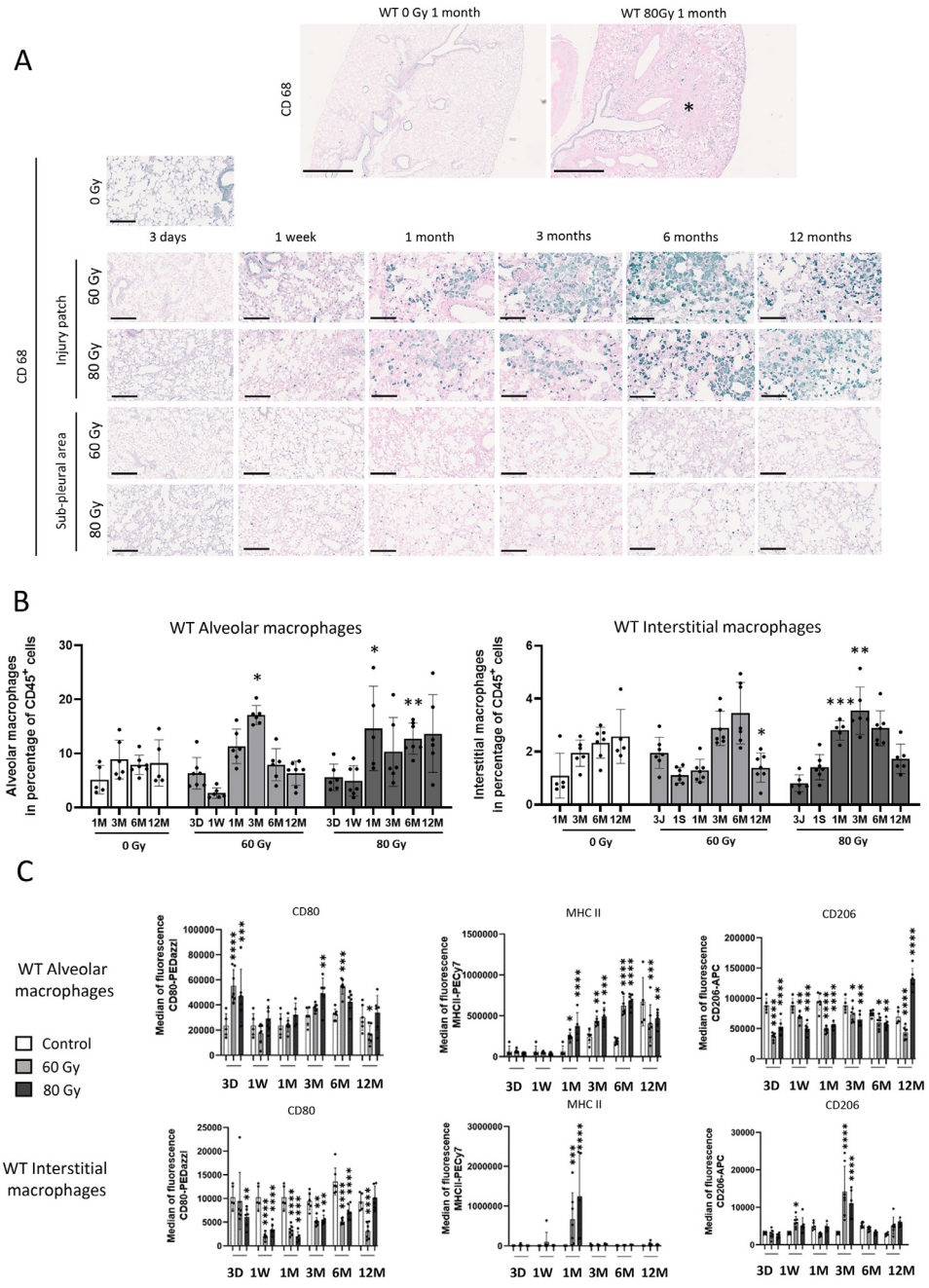

Fig. 1. Focal lung radiation exposure is associated with macrophage invasion. (A) Upper panel shows representative images of CD68 immunostaining (blue) in irradiated tissue 1-month post-80 Gy compared with age-matched control, showing that invading macrophages are located mainly around the injured area (*) (Scale bar = 1 mm). Lower panel shows representative pictures with higher magnification of CD68 immunostaining in control tissues and in irradiated ones 3 days, 1 week, and 1, 3, 6, and 12 months postexposure to 60 or 80 Gy, close to the injury patch and in subpleural area. Scale bar = 250 μm. Six < n < 8 animals per group. (B) Damaged area or corresponding zone in unirradiated lungs were digested and analyzed by flow cytometry. Number of alveolar macrophages (AM, $CD45^+/CD11b^{+/-}/CD68^+/Ly6c^{+/-}/CD11c^+/Siglec\ F^+$) and interstitial macrophages (IM, $CD45^+/CD11b^+/CD68^+/Ly6c^-/CD11c^-/Siglec\ F^-$), expressed as percentage of CD45-positive cells, in irradiated area 3 days (3D), 1 week (1W), 1 month (1M), 3 months (3M), 6 months (6M), and 12 months (12M) postexposure and in corresponding zone in unirradiated lungs from 1 to 12 months postexposure to 0, 60, or 80 Gy. One month control mice served as controls for 3D, 1W, and 1M time points. Five < n < 7 per group. *P < .05; **P < .01; ***P < .001. (C) Graphics showing the evolution of median fluorescence obtained by flow cytometry when staining AM and IM with CD80, MHC II, and CD206, from 3D to 12M postexposure to 60 or 80 Gy and from 1 to 12M in unirradiated tissues. One month control mice served as controls for 3D, 1W, and 1M time points. Five < n < 7 per group. *P < .05; **P < .01; ***P < .001; ****P < .0001.

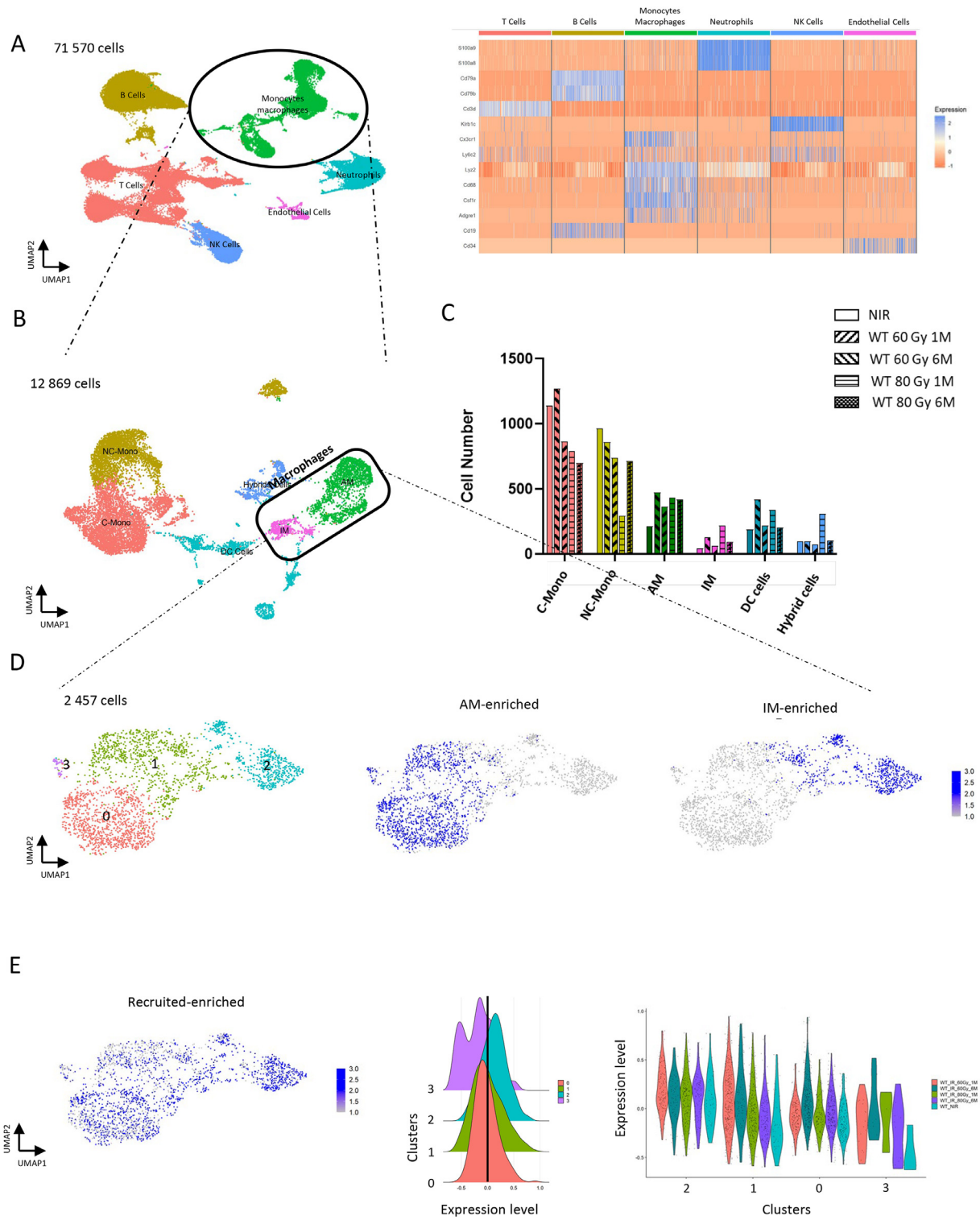

Fig. 2. Focal lung irradiation is associated with macrophage invasion showing recruited profile. (A) Global Uniform Manifold Approximation and Projection (UMAP) of 71,570 WT CD45^{+} cells obtained across all samples (left panel, downsampled to 14,314 cells per group, Louvain resolution 0.02) and heatmap visualization of markers identifying cell clusters in the global UMAP (right panel). (B) UMAP obtained following sub-clustering of 12,869 monocytes/macrophages cells (Louvain resolution 0.175). (C) Histogram showing monocytes/macrophages cell numbers in unirradiated tissues (NIR), 1 and 6 months following 60 Gy and 80 Gy radiation exposure. (D) New Seurat subobject including AM and IM from UMAP shown in B (2457 cells), showing 4 clusters (left panel, Louvain resolution 0.4), and projection of alveolar or interstitial scores as indicated (middle and right panels, concerned cells are shown in blue). E: Projection of recruited cells score on the UMAP Figure 2D (left panel, concerned cells in blue), and ridge and violin plots highlighting cluster 2 demonstrating a recruited profile (right panels).

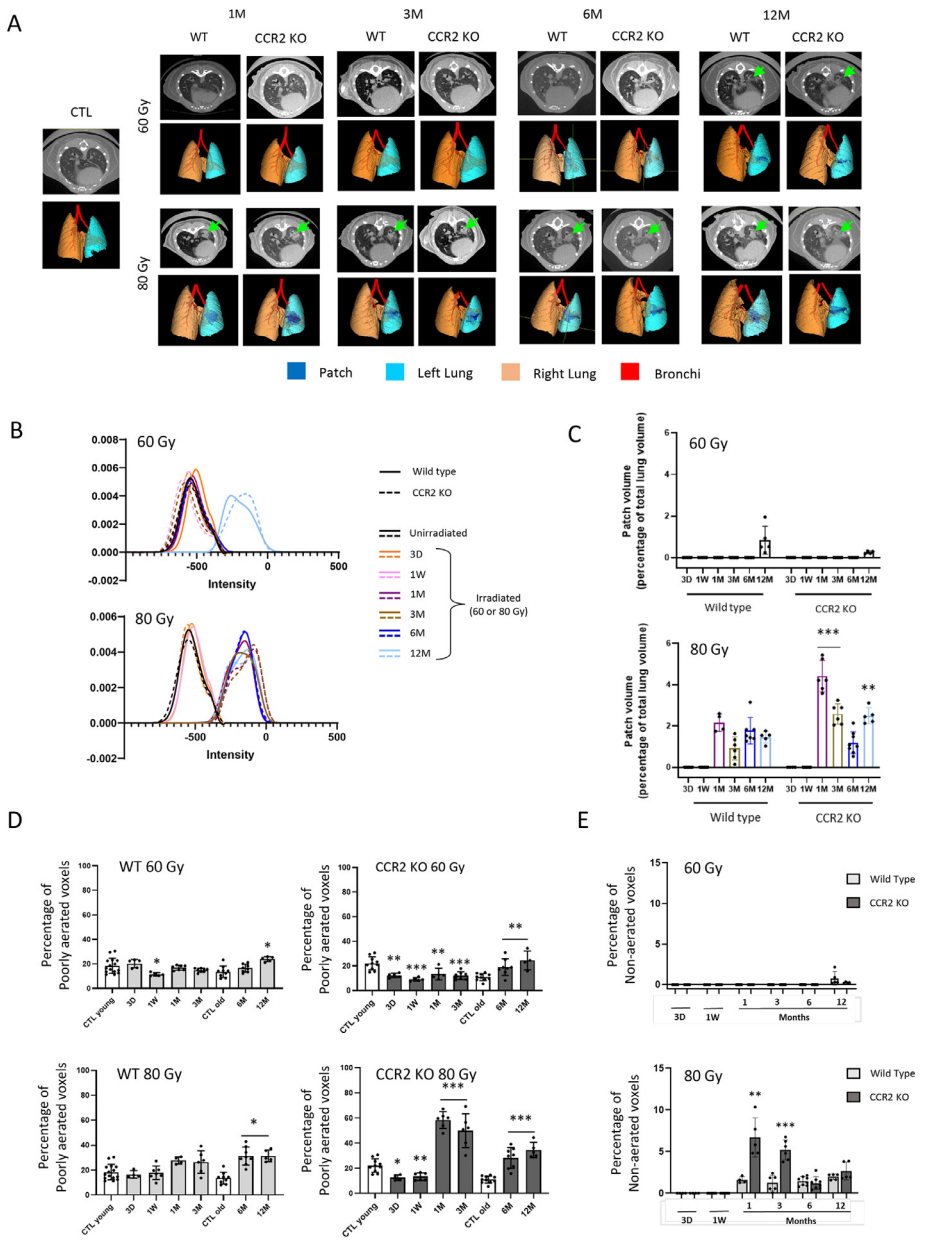

Fig. 3. Abrogation of CCR2-dependent monocyte recruitment does not impact radiation-induced lung damage development. (A) Representative microcomputed tomography images (upper lines) and 3-dimensional reconstructions (lower lines) in WT and CCR2 KO mice 1, 3, 6, and 12 months postexposure to 60 or 80 Gy. WT control images are given as examples and are not different between strains and all along the experimental period. Lung opacification is indicated by green arrows when present. For 3D reconstructions, different colors have been used to differentiate the injury patch (dark blue), left lung (light blue), right lung (orange), and bronchi (red). (B) Smoothed mean intensity representation in Hounsfield Units (HU) in the injured area (patch when visible, left lung otherwise) in WT and CCR2 KO mice 3 days (3D), 1 week (1W), and 1 (1M), 3 (3M), 6 (6M), and 12 months (12M) postexposure to 0, 60, or 80 Gy. (C) Volume of the injury patch as a percentage of total lung volume measured in WT and CCR2 KO mice from 3 days to 12 months postexposure to 60 (upper panel) and 80 Gy (lower panel). $^{**}P < .01$; $^{***}P < .001$ compared with time-matched patch volume in WT mice. Four < n < 7 per group. (D) Lung aeration volumes as indicated by percentage of poorly aerated volume ([−435, +500] HU) measured in the left lungs of control WT and CCR2 KO mice and at 3D, 1W and 1, 3, 6, and 12M postexposure to 60 Gy and 80 Gy. $^{*}P < .05$; $^{**}P < .01$; $^{***}P < .001$ compared with time-matched controls, that is, pooled young (1 and 3 months) or pooled old controls (6 and 12 months). Ten < n < 15 per control group; 4 < n < 8 per irradiated group. $^{*}P < .05$; $^{**}P < .01$; $^{***}P < .001$. (E) Percentage of nonaerated volume (more than −121 HU) measured in the left lungs of WT and CCR2 KO mice at 3D, 1W, and 1, 3, 6, and 12M postexposure to 60 Gy (upper panel) and 80 Gy (lower panel). $^{**}P < .01$, $^{***}P < .001$ compared with wild-type littermates. Four < n < 8 per group.

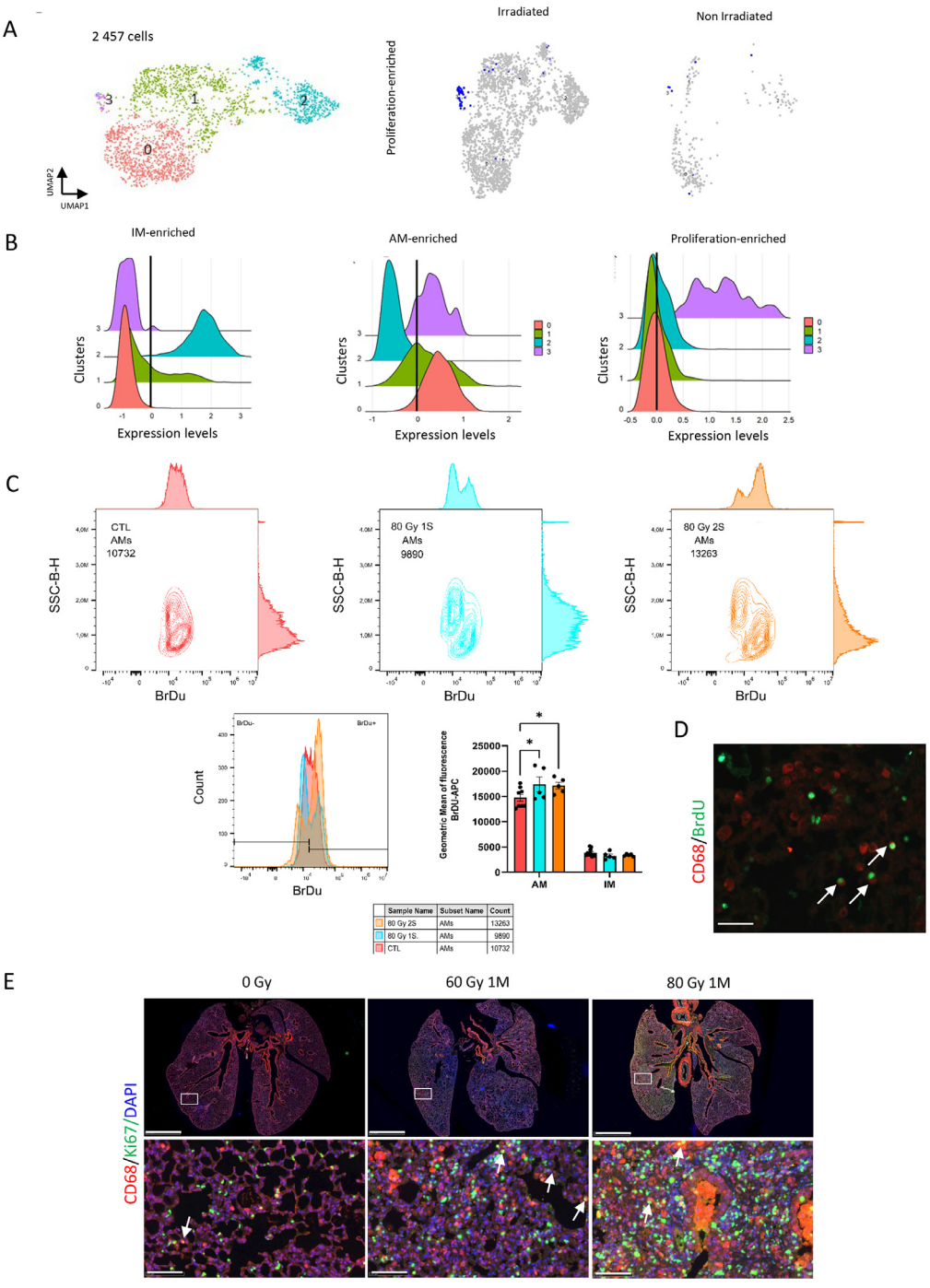

Fig. 4. A subpopulation of proliferating alveolar macrophages is present after radiation exposure. (A) Global Uniform Manifold Approximation and Projection (UMAP) of 2,457 WT macrophages showing 4 clusters (left panel, Louvain resolution 0.4). Middle and right panels show projection of proliferation score on the split UMAP (irradiated vs non irradiated, concerned cells in blue). (B) Ridge plots identifying cluster 2 as IM and clusters 0, 1, and 3 as AM (left and middle panels, respectively), and AM cluster 3 as a proliferating cluster (right panel). (C) Flow cytometry analyses: Representative graph of Side Scatter (SSC) versus BrdU for unirradiated tissue, and 1 and 2 weeks post-80 Gy (upper panel). Geometric means of BrdU-specific antibody in control compared with irradiated tissues 1 and 2 weeks post-80 Gy (left lower panel) and fluorescence quantification in AM and IM (right lower panel). (D) Representative image of BrdU/CD68 co-immunostaining on irradiated lung tissue 2 weeks post-80 Gy showing double-stained proliferating macrophages. Scale bar = 50 μm. (E) Representative image of Ki67/CD68 co-immunostaining performed in unirradiated tissues and 1-month post-60 or 80 Gy exposure showing several double-stained proliferating macrophages (white arrows). Global view: scale bar = 2.5mm, details: scale bar = 100 μm.

HU curve construction confirmed tissue densification with no difference between strains (Fig. 3B). No significant difference in patch volume was observed between strains post-60 Gy exposure (Fig. 3C, upper panel) The patch was significantly larger in CCR2 KO mice 1, 3, and 12 months post-80 Gy (Fig. 3C, bottom panel).

HU thresholds were applied to the whole left lung to discriminate between normoaerated ([−900, −435] HU), poorly aerated ([−435, −121] HU), and nonaerated volumes (more than −121 HU). For more clarity, graphs were generated using pooled controls (Fig. E5A). Focal lung exposure to 60 Gy generated a slight decrease in poorly aerated volumes at 1 month in WT mice but a lasting decrease in CCR2 KO mice (Fig. 3D, upper panels). An increase in poorly aerated volumes occurred only at 12 months in WT mice and from 6 months in CCR2 KO mice. Post-80 Gy (Fig. 3D, lower panels), poorly aerated volumes were increased at 6 and 12 months in WT mice. CCR2 KO mice demonstrated a very acute (3 days and 1 week) decrease followed by a significant increase in poorly aerated volumes from 1 to 12 months postexposure. Nonaerated volumes showed no convincing changes following 60 Gy exposure (Fig. 3E, upper panel). After 80 Gy (lower panel), the percentage of nonaerated volumes increased from 1 to 12 months in both mouse strains, with significantly more volume concerned in CCR2 KO mice at 1 and 3 months.

Anatomopathological observations demonstrate similar acute and late radiation-induced lung damage in both CCR2 KO and WT mice

Similar observations were done postirradiation when examining tissue Hemalun-Eosin-Saffron (HES) sections in both mouse strains (Fig. E5B-D). The thickness of alveolar septa (Fig. E6A), macrophage staining intensity (Fig. E6B), and macrophage numbers (Fig. E7) showed similar variations in both mouse strains.

RNA-seq analyses demonstrate similar cell populations in both CCR2 KO and WT mice

As for WT mice, 40,802 viable $CD45^+$ leucocytes were analyzed by single-cell RNA-seq, from lungs of unirradiated and 60 Gy-irradiated CCR2 KO mice, 1 and 6 months post-exposure (downsampled to 35,595 cells with 11,865 cells per group). We identified several known $CD45^+$ cells with the discrimination of 7 different cell types (Fig. E8A, left panel). Canonical markers are indicated Figure E8A, right panel. Monocytes and macrophages (3304 cells) were subclustered in 10 different cell populations shown in Figure E8B. We next focused on AM and IM macrophages (identified in Fig. E8C) and obtained a new UMAP containing 834 macrophages with 5 clusters shown in Figure E8D. We then applied the same scores as applied in the WT mice study (Fig. E4) to identify AM (clusters 0, 1, 3, and part of 4) and IM (cluster 2 and part of 4) in this new UMAP (concerned cells in blue, Fig. E8D, middle and right panels, respectively). The recruited macrophage score (Fig. E8E, left panel) identifies both IM and AM. The ridge plot shows that clusters 2 and 4 demonstrate a recruited profile (Fig. E8E, right panel). These results suggest that a proportion of macrophages reach the damaged lung area probably via a CCR2-independent pathway.

A WT proliferating AM population is present lung tissue postirradiation

On the WT macrophage UMAP (2,457 cells, Fig. 4A, left panel), projection of a score based on genes expressed by proliferating cells (score details in Fig. E4C) highlighted cluster 3 as a proliferating cluster in control and irradiated tissues (Fig. 4A, right and middle panels, respectively). Cluster 3 was identified as an alveolar/proliferating macrophage cluster as shown by ridge plots in Figure 4B. BrdU staining analyzed by flow cytometry confirmed the presence of proliferating AM in both control and irradiated tissues (Fig. 4C). Representative images of BrdU staining are given in Figure 4D. To support BrdU data, Ki67/CD68 co-immunostaining was performed on all tissue samples and showed the presence of numerous double-positive proliferating macrophages in the radiation-damaged area compared with control tissues (Fig. 4E).

Irradiation generates WT AM metabolic reprogramming over time possibly from proliferating AM

To go further, we chose to come back to the global WT UMAP, without downsampling, to keep access to all WT AM. This resulted in a UMAP gathering of 90,870 $CD45^+$ cells from all WT samples (Fig. 5A, left panel). Projection of the AM score identified cluster 12 as AM (Fig. 5A, right panel). The 2714 AM were subclusterized, giving 5 different clusters (Fig. 5B, left panel), among which cluster 3 was identified as a hybrid cluster. We then decided to pursue after elimination of this hybrid cluster and obtained a UMAP gathering of 2499 AM shown according to the groups in Fig. 5B, right panel. Using the Monocle3 package on R,[24] we constructed a pseudotemporal ordering of individual cells (pseudotime single-cell trajectory), choosing the proliferating AM cluster as the starting point (Fig. 5B, left panel). Trajectory is shown alone and according to the pseudotime and the groups in Figure 5C (middle and right panels). Trajectory originating from proliferating AM shows that AM evolve through an acute transcriptomic profile common to 60 and 80 Gy exposures and then reveals the possibility of 2 different branches (node 3), 1 gathering AM post-60 Gy exposure (leaf 3), the other one gathering AM post-80 Gy exposure (leaf 4). Interestingly, leaf 2 identifies very early in the pseudotime a subgroup of AM evolving

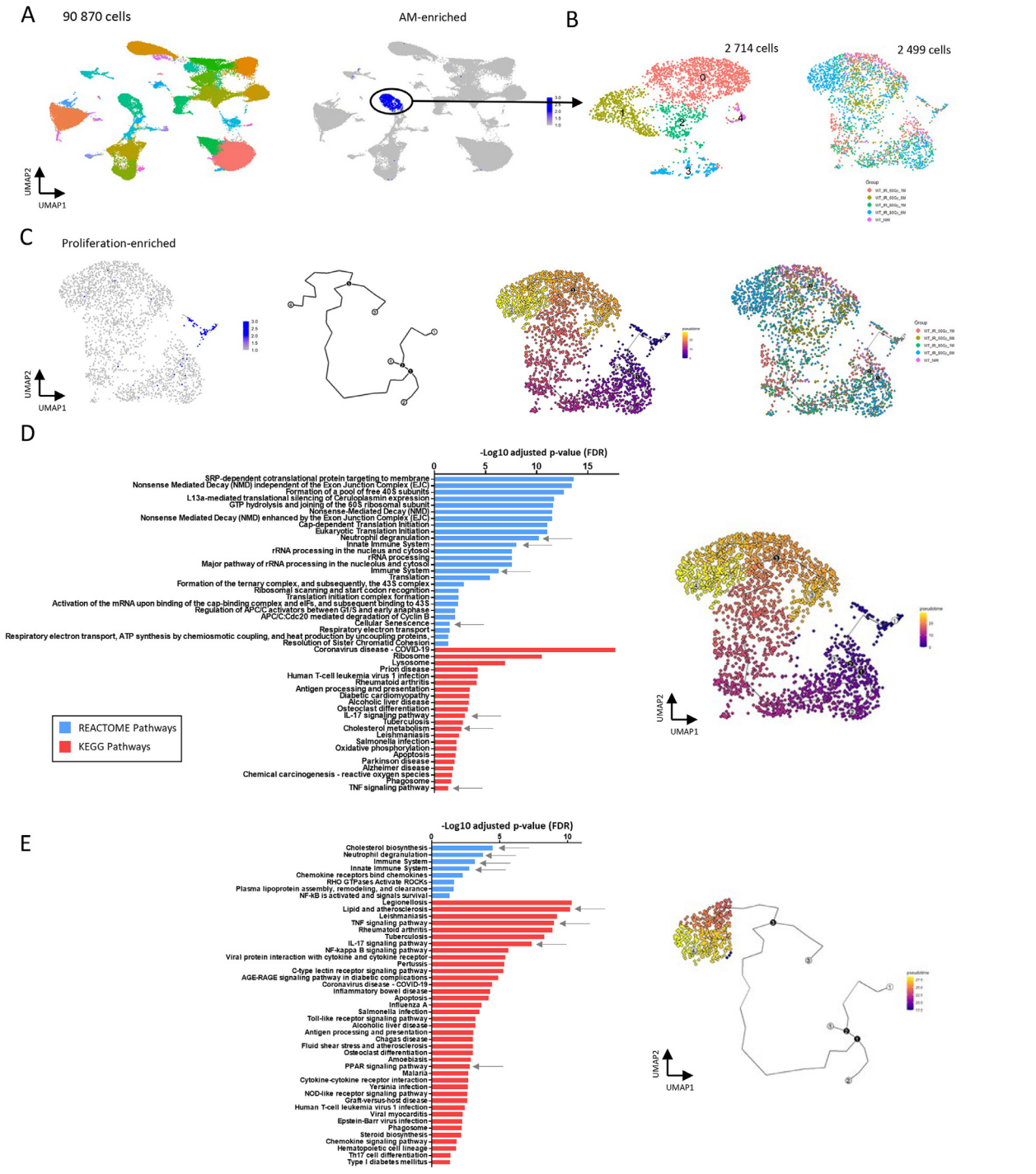

Fig. 5. Transcriptome reprogramming of WT alveolar macrophages following radiation exposure. (A) Uniform Manifold Approximation and Projection (UMAP) of 90,870 WT CD45^{+} cells obtained across all samples (WT NIR: 14,314 cells; WT 60 Gy 1M: 14,397 cells; WT 60 Gy 6M: 17,961 cells; WT 80 Gy 1M: 14,958 cells; and WT 80 Gy 6M: 29,240 cells, left panel, Louvain resolution 0.5). Projection of AM score highlighting cluster 12 (right panel, concerned cells are indicated in blue). (B) Subclusterization of cluster 12, including AM and hybrid cells (left panel, Louvain resolution 0.2). Right panel shows UMAP excluding hybrid cells (2,499 alveolar macrophages). (C) From left to right: projection of proliferation score on AM UMAP, proliferating cells are shown in blue; pseudotime analysis showing the main path leading to macrophages typical of late time points; UMAP visualization is shown according to the pseudotime and according to the groups. (D and E) In-depth analysis using the Moran's I test function showing genes that change in expression as a function of pseudotime. This method made it possible to find and classify genes that are differentially expressed across the single-cell trajectory, on the entire trajectory (D) or on only part of the trajectory focusing on some of the cells, here the 80 Gy 6M (E).

through a transcriptomic profile encountered 6M post-80 Gy. Next, we used the graph_test function to identify and classify genes that change in expression as a function of pseudotime (the Moran's I test) either on the entire trajectory (Fig. 5D, Tables E1 and E2) or on some of the cells, here AM post-80 Gy cells (Fig. 5E, Tables E3 and E4). The top 300 genes of each analysis were used for functional enrichment analysis. Results showed for the entire trajectory that terms linked to "immune system," "innate immune system," "cellular senescence," "Il-17 signaling," and "cholesterol metabolism" are very well classified. Interestingly, when focusing on AM post-80 Gy cells, functional terms linked to "cholesterol metabolism" and "lipid and atherosclerosis" emerge on the top. Altogether, these results strongly suggest a lipid- and cholesterol-associated metabolic shift of AM after SBRT. To confirm these findings, fatty acid metabolism and cholesterol biosynthesis scores (details in Fig. E4B) were projected on the AM UMAP (Fig. 6, concerned cells in blue). AM from 1M time points post 60 and 80 Gy were characterized by fatty acid metabolism (Fig. 6A, left panel, confirmed by immunofluorescence and macrophages proportions in the right panels), whereas AM 6M were characterized by cholesterol biosynthesis gene expression (Fig. 6B, left panel, confirmed by immunofluorescence and macrophages proportions in the right panels). Interestingly, the cluster associated with leaf 4 in the pseudotime responds to the senescence associated secretory phenotype (SASP) score, suggesting the emergence of senescent AM 6M after 80 Gy exposure (Fig. 6C). Details of the numbers of cells analyzed per slide are given in table and Figure 6D for macrophages quantification.

Discussion

Pulmonary macrophages are considered the first line of defense in cases of lung trauma and may represent a promising therapeutic target against RILF.[25] The lung is a parallel-organized organ with functioning reserve capacity, and we know that the volume exposed to ionizing radiation is a determinant factor governing the likelihood of developing RILF. In the present study, we challenged knowledge about the role of macrophages in RILF in an original preclinical model of mouse focal lung irradiation. The doses used in the present study come from previous studies using focal lung irradiation with the same beam collimation.[16,17] Reducing volume exposition necessitates increasing the dose delivered to induce tissue damage compared with whole thorax exposures, as shown also by previous studies from other laboratories.[26-28] Some limits are inevitably inherent to our model, that is, focal irradiation using arc-based dose delivery is associated with dose deposition beyond the arc and results in heterogeneous dose distribution. Despite these limits, we are strongly convinced that our model offers accurate clinical exposure miming the reduction of exposed volume compared with whole thorax irradiation, and the heterogeneity of dose distribution is observed in the clinic.[16] Furthermore, it is interesting to note that the doses of 60 and 80 Gy in the present study are very close to the very recent elegant study published by Farh et al[29] using 65 and 75 Gy focal lung exposure (single beam, 3 mm cone size), even with different dose delivery modalities. They demonstrate with interesting arguments that 65 Gy is probably the best single dose for further studies using restricted volume irradiation in rodents to decipher mechanisms of 2-month-based RILF. In our opinion, however, there is still an interesting debate especially concerning the time laps needed to develop lung fibrosis, that is, is the faster the best option? This guarantees future exciting projects.

We showed that focal irradiation of the lung was associated with M1-like AM and M2-like IM invasion near the irradiated area, confirming previous observations from our laboratory.[14] IM recruitment persists in a CCR2-independent manner, and RILF development may also implicate a population of proliferating resident AM as part of a metabolic shift toward cholesterol biosynthesis and senescent phenotype. In our original results obtained by single-cell RNA sequencing, we observed that both AM and IM populations were increased, both partly concerned by the recruited gene expression profile. Mice overexpressing IL10 show spontaneous lung fibrosis development, associated with M2 macrophage activation via a CCL2/CCR2 signaling axis.[30] CCR2 KO mice are protected from Fluorescein Iso-Thiocyanate- and bleomycin-induced pulmonary fibrosis[31] and $CCR2^{+}$-infiltrating monocyte-derived macrophages have been shown to participate in RILF following WTI in mice.[12] This drove us to verify the hypothesis of CCR2-dependent monocyte recruitment in our model. Surprisingly, CCR2 KO mice experienced radiation-induced lung damage very similar to their WT littermates. Although challenging, CT imaging is part of the basic diagnostic armamentarium in patients with radiation-induced fibrosis.[32] In preclinical studies, the CT scan is an interesting noninvasive technique,[33] but its use can be complicated, especially with the absence of observable well-defined clinical features, given the small size of the mouse lungs.[34] We therefore applied thresholds, based on the literature, to discriminate normo-, poorly, and nonaerated volumes and improve analysis accuracy.[19] We observed slight differences between strains, with especially lower HU values in CCR2 KO mice; however, these never reached values classically associated with emphysema. Higher percentages of poorly and nonaerated volumes were also observed at 1 and 3 months post-80 Gy in CCR2 KO mice, reflecting an increase in injury patch volume. Globally, abrogating CCR2-dependent monocyte recruitment had no obvious impact on lung damage severity in our model, suggesting a CCR2-independent monocyte recruitment process. Other pathways may be implicated in monocyte recruitment,[35] such as the CX3CL1-CX3CR1 axis as demonstrated in immune-mediated lung disease in mice.[36] This may be supported by the presence of "recruited" gene profile macrophages in CCR2 KO mice in our study.

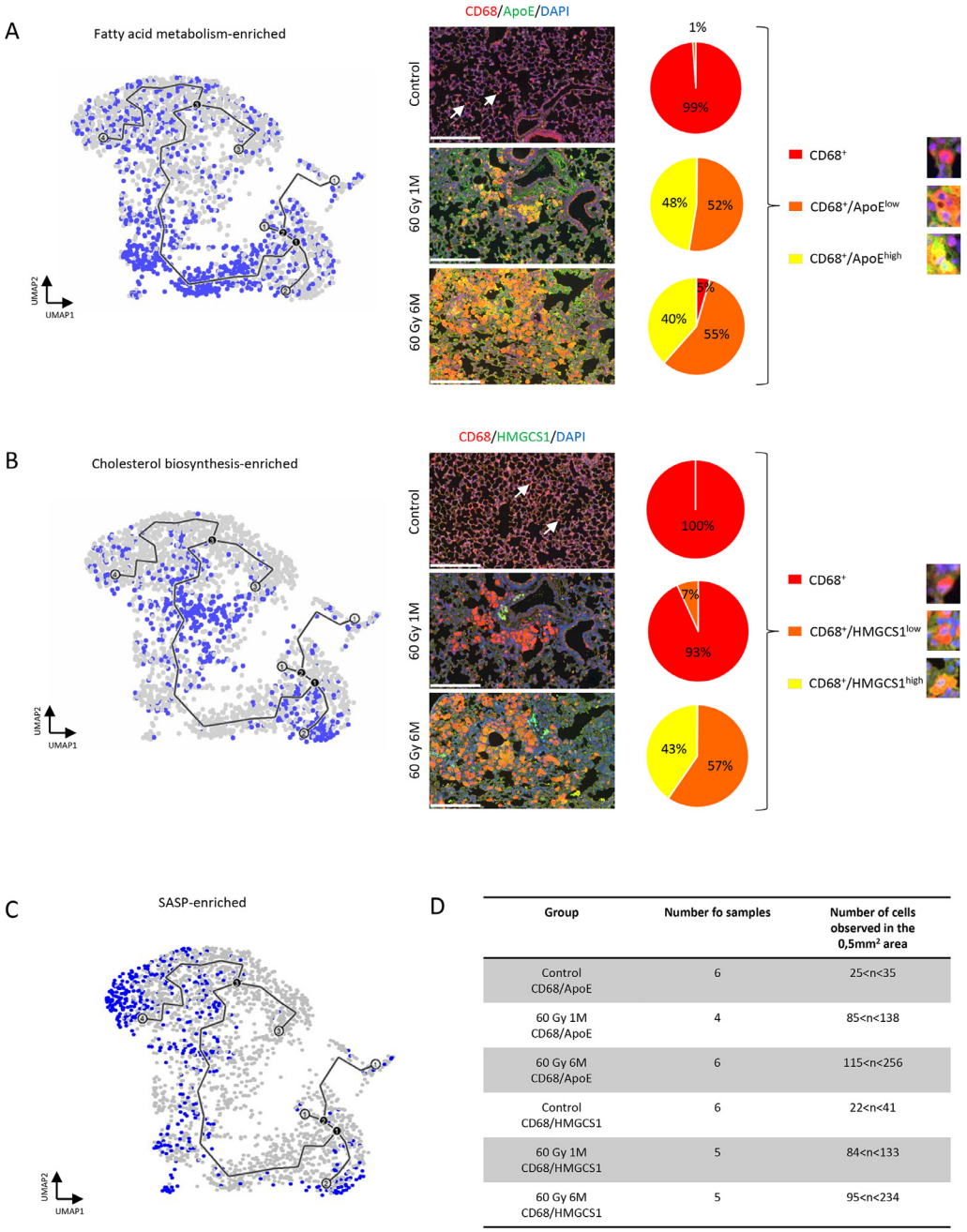

D

Group	Number fo samples	Number of cells observed in the 0,5mm² area
Control CD68/ApoE	6	25<n<35
60 Gy 1M CD68/ApoE	4	85<n<138
60 Gy 6M CD68/ApoE	6	115<n<256
Control CD68/HMGCS1	6	22<n<41
60 Gy 1M CD68/HMGCS1	5	84<n<133
60 Gy 6M CD68/HMGCS1	5	95<n<234

Fig. 6. Metabolic shift of alveolar macrophages following radiation exposure. (A) Projection of fatty acid metabolism score on AM UMAP (left panel, concerned cells in blue) superimposed with pseudotime trajectory revealing acute (1M) post-60 and 80 Gy clusters concerned with fatty acid metabolism profile. Right panel: representative images of unirradiated lung and irradiated lungs 1 and 6M post-60 Gy irradiation of CD68 (red)/ApoE (green) co-immunostaining highlighting double-stained macrophages. Scale bar = 250μm. Pie charts show CD68^{+}, CD68^{+}/ApoE^{low}, and CD68^{+}/ApoE^{high} macrophage proportions in percentage of total cells observed in a 0.5 mm^{2} area. (B) Projection of cholesterol biosynthesis score on AM UMAP (left panel, concerned cells in blue) superimposed with pseudotime trajectory revealing chronic (6M) post-60 and 80 Gy clusters concerned with cholesterol biosynthesis profile. Right panel: representative images of unirradiated lung and irradiated lungs 1 and 6M post-60 Gy irradiation of CD68 (red)/HMGCS1 (green) co-immunostaining highlighting double-stained macrophages. Scale bar = 250 μm. Pie charts show CD68^{+}, CD68^{+}/HMGCS1^{low}, and CD68^{+}/HMGCS1^{high} macrophage proportions in percentage of total cells observed in a 0.5 mm^{2} area. (C) Projection of SASP score on AM UMAP (left panel, concerned cells in blue) superimposed with pseudotime trajectory revealing chronic (6M) post-60 and 80 Gy clusters concerned with senescence profile. (D) Table highlighting the number of samples analyzed per group and the range of cell numbers observed per slide to obtain macrophage proportions shown in (A) and (B).

Interestingly, the demonstration of a role for recruited macrophages following WTI is associated with a role for interstitial subsets.[8,37] In our case, HES observations show numerous clusters of AM, also concerned by the recruited gene expression profile. It is conceivable that these AM may also come from recruited cells, because IM may be considered by some authors as the intermediaries between recruited macrophages and AM.[38] AM have also been shown to be able to move from one alveolus to another to prevent unnecessary inflammation and ensure lung homeostasis.[39] In our model exposing 4% of the total lung volume, numerous macrophages reside in unirradiated areas and may migrate through the damaged zone, explaining possible recruitment-independent increased macrophage populations. Further studies will be necessary to examine the existence of these migrating macrophages and find out whether they may express a "recruited" gene profile.

We also identified a proliferating small population of macrophages. Resident macrophage proliferation has been demonstrated in idiopathic pulmonary fibrosis[40] and may contribute to lung damage in the context of focal radiation exposure. Moreover, pseudotime trajectories revealed that this proliferating subpopulation of macrophages may switch their metabolism through cholesterol biosynthesis, a possible reason for foam cell generation, including in the case of CCR2-dependent monocyte recruitment abrogation.[41] AM clusters on HES tissue sections show numerous lipid-laden foam cells following radiation exposure in our model. Farh et al[29] also observed an enrichment of lipid metabolism-related processes at 6 weeks following 75 Gy focal lung exposure and observed foamy macrophages on lung tissue sections. Imbalance in lipid metabolism may exacerbate tissue fibrotic reaction, and modifications of AM lipid metabolism have been associated with various pulmonary pathologies such as asthma, chronic obstructive pulmonary disease, or idiopathic fibrosis[42-45] and in preclinical models of lung damage, including radiation exposure.[46] They may be implicated in lung damage following focal irradiation. Finally, our data also suggest the evolution of subsets of macrophages toward an elevated SASP mRNA expression 6M following 80 Gy exposure. This is in accordance with previous studies, suggesting a potential role for senescent macrophages in RILF.[15]

In conclusion, our paper provides new data on the possible roles of macrophages in RILF, using an original preclinical model of limited lung volume exposure that accurately mimes clinical conditions. Even if further validation remains necessary, this highlights the importance of considering results depending on the preclinical model used and calls for extensive future studies to decipher the roles of macrophages in the development of lung focal radiation damage, especially concerning dysregulated cell metabolism that may open new therapeutic avenues in this context.

References

1. Giuranno L, Ient J, De Ruysscher D, et al. Radiation-induced lung injury (rili). *Front Oncol* 2019;9:877.
2. Rahi MS, Parekh J, Pednekar P, et al. Radiation-induced lung injury-current perspectives and management. *Clin Pract* 2021;11:410-429.
3. Almeida C, Nagarajan D, Tian J, et al. The role of alveolar epithelium in radiation-induced lung injury. *PloS one* 2013;8:e53628.
4. Choi SH, Hong ZY, Nam JK, et al. A hypoxia-induced vascular endothelial-to-mesenchymal transition in development of radiation-induced pulmonary fibrosis. *Clini Cancer Res* 2015;21:3716-3726.
5. Su L, Dong Y, Wang Y, et al. Potential role of senescent macrophages in radiation-induced pulmonary fibrosis. *Cell Death Dis* 2021;12:527.
6. Aegerter H, Lambrecht BN, Jakubzick CV. Biology of lung macrophages in health and disease. *Immunity* 2022;55:1564-1580.
7. Arora S, Dev K, Agarwal B, et al. Macrophages: their role, activation and polarization in pulmonary diseases. *Immunobiology* 2018;223:383-396.
8. Meziani L, Mondini M, Petit B, et al. Csf1r inhibition prevents radiation pulmonary fibrosis by depletion of interstitial macrophages. *Eur Resp J* 2018;51.
9. Lavigne J, Soysouvanh F, Buard V, et al. Conditional plasminogen activator inhibitor type 1 deletion in the endothelial compartment has no beneficial effect on radiation-induced whole-lung damage in mice. *Int J Radiation Oncol, Biol, Phys* 2017;99:972-982.
10. Groves AM, Johnston CJ, Misra RS, et al. Whole-lung irradiation results in pulmonary macrophage alterations that are subpopulation and strain specific. *Radiat Res* 2015;184:639-649.
11. de Leve S, Wirsdorfer F, Cappuccini F, et al. Loss of cd73 prevents accumulation of alternatively activated macrophages and the formation of prefibrotic macrophage clusters in irradiated lungs. *FASEB J* 2017;31:2869-2880.
12. Groves AM, Johnston CJ, Williams JP, et al. Role of infiltrating monocytes in the development of radiation-induced pulmonary fibrosis. *Radiat Res* 2018;189:300-311.
13. Butterworth KT. Evolution of the supermodel: progress in modelling radiotherapy response in mice. *Clin Oncol (R Coll Radiol)* 2019;31:272-282.
14. Lavigne J, Suissa A, Verger N, et al. Lung stereotactic arc therapy in mice: development of radiation pneumopathy and influence of hif-1alpha endothelial deletion. *Int J Rad Oncol, Biol, Phys* 2019;104:279-290.
15. Soysouvanh F, Benadjaoud MA, Dos Santos M, et al. Stereotactic lung irradiation in mice promotes long-term senescence and lung injury. *Int J Radiat Oncol, Biol, Phys* 2020;106:1017-1027.
16. Bertho A, Dos Santos M, Buard V, et al. Preclinical model of stereotactic ablative lung irradiation using arc delivery in the mouse: effect of beam size changes and dose effect at constant collimation. *Int J Rad Oncol, Biol, Phys* 2020;107:548-562.
17. Bertho A, Dos Santos M, Braga-Cohen S, et al. Preclinical model of stereotactic ablative lung irradiation using arc delivery in the mouse: Is fractionation worthwhile? *Front Med* 2021;8 794324.
18. Ma CM, Coffey CW, DeWerd LA, et al. Aapm protocol for 40-300 kv x-ray beam dosimetry in radiotherapy and radiobiology. *Med Phys* 2001;28:868-893.
19. Ruscitti F, Ravanetti F, Bertani V, et al. Quantification of lung fibrosis in ipf-like mouse model and pharmacological response to treatment by micro-computed tomography. *Fronti Pharmacol* 2020;11:1117.
20. Mecozzi L, Mambrini M, Ruscitti F, et al. In-vivo lung fibrosis staging in a bleomycin-mouse model: a new micro-CT guided densitometric approach. *Sci Rep* 2020;10:18735.
21. Zaynagetdinov R, Sherrill TP, Kendall PL, et al. Identification of myeloid cell subsets in murine lungs using flow cytometry. *Am J Resp Cell Mol Bio* 2013;49:180-189.
22. Misharin AV, Morales-Nebreda L, Mutlu GM, et al. Flow cytometric analysis of macrophages and dendritic cell subsets in the mouse lung. *Am J Respir Cell Mol Biol* 2013;49:503-510.

23. Butler A, Hoffman P, Smibert P, et al. Integrating single-cell transcriptomic data across different conditions, technologies, and species. *Nat Bio* 2018;36:411-420.
24. Trapnell C, Cacchiarelli D, Grimsby J, et al. The dynamics and regulators of cell fate decisions are revealed by pseudotemporal ordering of single cells. *Nat Bio* 2014;32:381-386.
25. Meziani L, Deutsch E, Mondini M. Macrophages in radiation injury: a new therapeutic target. *Oncoimmunology* 2018;7 e1494488.
26. Hong ZY, Lee CG, Shim HS, et al. Time, dose, and volume responses in a mouse pulmonary injury model following ablative irradiation. *Lung* 2016;194:81-90.
27. Hong ZY, Eun SH, Park K, et al. Development of a small animal model to simulate clinical stereotactic body radiotherapy-induced central and peripheral lung injuries. *J Radiat Res* 2014;55:648-657.
28. Cho J, Kodym R, Seliounine S, et al. High dose-per-fraction irradiation of limited lung volumes using an image-guided, highly focused irradiator: simulating stereotactic body radiotherapy regimens in a small-animal model. *Int J Radiat Oncol Biol Phys* 2010;77:895-902.
29. Farh ME, Kim HJ, Kim SY, et al. Transcriptional changes in radiation-induced lung injury: A comparative analysis of two radiation doses for preclinical research. *Int J Mol Sci* 2024;25.
30. Sun L, Louie MC, Vannella KM, et al. New concepts of il-10-induced lung fibrosis: fibrocyte recruitment and m2 activation in a ccl2/ccr2 axis. *Am J Physiol Lung Cell Mol Physiol* 2011;300:L341-L353.
31. Moore BB, Paine 3rd R, Christensen PJ, et al. Protection from pulmonary fibrosis in the absence of ccr2 signaling. *J Immunol* 2001;167:4368-4377.
32. Frakulli R, Salvi F, Balestrini D, et al. Radiological differential diagnosis between fibrosis and recurrence after stereotactic body radiation therapy (sbrt) in early stage non-small cell lung cancer (nsclc). *Transl Lung Cancer Res* 2017;6:S1-S7.
33. van Berlo D, Khmelinskii A, Gasparini A, et al. Micro cone beam computed tomography for sensitive assessment of radiation-induced late lung toxicity in preclinical models. *Radiotherapy and oncology: journal of the European Society for Therapeutic Radiology and Oncology* 2019;138:17-24.
34. De Ruysscher D, Granton PV, Lieuwes NG, et al. Nintedanib reduces radiation-induced microscopic lung fibrosis but this cannot be monitored by ct imaging: a preclinical study with a high precision image-guided irradiator. *Radiother Oncol* 2017;124:482-487.
35. Shi C, Pamer EG. Monocyte recruitment during infection and inflammation. *Nat Rev Immunol* 2011;11:762-774.
36. Zhang J, Patel JM. Role of the cx3cl1-cx3cr1 axis in chronic inflammatory lung diseases. *Int J Clin Exp Med* 2010;3:233-244.
37. Hanania AN, Mainwaring W, Ghebre YT, et al. Radiation-induced lung injury: assessment and management. *Chest* 2019;156:150-162.
38. Schyns J, Bureau F, Marichal T. Lung interstitial macrophages: past, present, and future. *J Immunol Res* 2018;2018 5160794.
39. Neupane AS, Willson M, Chojnacki AK, et al. Patrolling alveolar macrophages conceal bacteria from the immune system to maintain homeostasis. *Cell* 2020;183 110-125 e11.
40. Morse C, Tabib T, Sembrat J, et al. Proliferating spp1/mertk-expressing macrophages in idiopathic pulmonary fibrosis. *Eur Respir J* 2019;54.
41. Keidar S, Attias J, Heinrich R, et al. Angiotensin ii atherogenicity in apolipoprotein e deficient mice is associated with increased cellular cholesterol biosynthesis. *Atherosclerosis* 1999;146:249-257.
42. Ogger PP, Byrne AJ. Macrophage metabolic reprogramming during chronic lung disease. *Mucosal Immunol* 2021;14:282-295.
43. Hsieh MH, Chen PC, Hsu HY, et al. Surfactant protein d inhibits lipid-laden foamy macrophages and lung inflammation in chronic obstructive pulmonary disease. *Cell Mol Immunol* 2023;20:38-50.
44. Hirama N, Shibata Y, Otake K, et al. Increased surfactant protein-d and foamy macrophages in smoking-induced mouse emphysema. *Respirology* 2007;12:191-201.
45. Romero F, Shah D, Duong M, et al. A pneumocyte-macrophage paracrine lipid axis drives the lung toward fibrosis. *Am J Respir Cell Mol Biol* 2015;53:74-86.
46. Curras-Alonso S, Soulier J, Defard T, et al. An interactive murine single-cell atlas of the lung responses to radiation injury. *Nat Commun* 2023;14:2445.